

STEADY STATE PENETRATION OF COMPRESSIBLE RIGID PERFECTLY PLASTIC TARGETS

R. C. BATRA and T. GOBINATH

Department of Engineering Mechanics, University of Missouri-Rolla, Rolla, MO 65401-0249, U.S.A.

Abstract—Steady state axisymmetric deformations of a homogeneous, isotropic, compressible and rigid perfectly plastic target being penetrated by a rigid cylindrical penetrator with a hemispherical nose are studied by the finite element method. The steady state is reached with respect to an observer situated on the penetrator nose and moving with it. Tillotson's equation, restricted to mechanical deformations, is used to express the pressure as a function of the mass density. Contact between the penetrator and the target is assumed to be smooth. The effect of compressibility of the material is delineated by comparing results for compressible and incompressible materials. Also studied is the effect of the penetrator speed on target deformations.

INTRODUCTION

In an attempt to shed some light on the validity of the approximations made in simple theories of penetration due to Alekseevskii [1] and Tate [2], and to understand better the significance of various kinematic variables, Batra and Wright [3] studied in detail a steady state penetration problem that simulates the following situation. Suppose that the penetrator is in the intermediate stages of penetration so that the active target/penetrator interface is at least one or two penetrator diameters away from either target face, and the remaining penetrator is much longer than several diameters and is still travelling at a uniform speed. This stage of penetration can be idealized as one in which deformations of the target appear to be steady to an observer situated on the penetrator nose. Wright and Batra [3] presumed that the target is made of a rigid/perfectly plastic material, and is being penetrated by a long cylindrical rigid rod with a hemispherical nose. Subsequently Batra [4] showed that the axial resisting force experienced by the rigid penetrator is considerably reduced if its nose shape is ellipsoidal rather than hemispherical and also investigated the effect of the dependence of the flow stress upon the strain-rate. He [5] has extended this work to the case when the target material is thermally softening but strain and strain-rate hardening.

Pidsley [6] recently studied a complete penetration problem in which both target and penetrator materials were assumed to be compressible rigid/perfectly plastic. Whereas he gave a detailed numerical solution for one set of material and geometric parameters, we study the steady state penetration problem similar to the one analyzed by Batra and Wright [3] and investigate the effect of the speed of the penetrator and the compressibility of the target material. We hope that the kinematic and stress fields found in this study will be useful in identifying key variables to be included in simpler engineering theories of target penetration. Since the continuity equation has no diffusive term, it is more challenging to solve the problem numerically for compressible materials. Pidsley used the finite difference code HELP developed by Hageman and Walsh [7] to solve the problem. However, we use the finite element method and have developed the requisite code.

We note that no failure or fracture criterion is included in our study. Thus the target material is assumed to undergo unlimited amount of deformations.

FORMULATION OF THE PROBLEM

We describe the axisymmetric deformations of the target with respect to a set of cylindrical coordinate axes with origin at the center of the hemispherical nose of the rigid penetrator and z-axis pointing into the target. Equations governing the steady-state deformations of the target

are

$$\operatorname{div}(\rho \mathbf{v}) = 0, \quad (1.1)$$

$$\operatorname{div} \boldsymbol{\sigma} = \rho(\mathbf{v} \cdot \operatorname{grad})\mathbf{v}. \quad (1.2)$$

Here ρ is the current mass density of a target material particle, \mathbf{v} is the velocity relative to an observer situated on the penetrator nose tip and moving with it, $\boldsymbol{\sigma}$ is the Cauchy stress tensor, and the operators grad and div signify the gradient and divergence operators on fields defined in the present configuration. Equations (1.1) and (1.2) express, respectively, the balance of mass and the balance of linear momentum with zero body forces.

We presume that the target material is compressible and obeys the Von-Mises yield criterion and the associated flow rule. That is†

$$\boldsymbol{\sigma} = -p(\rho)\mathbf{1} + \frac{\sigma_0}{\sqrt{3}I} \bar{\mathbf{D}}, \quad (2.1)$$

$$\bar{\mathbf{D}} = \mathbf{D} - \frac{1}{3}(\operatorname{tr} \mathbf{D})\mathbf{1}, \quad (2.2)$$

$$\mathbf{D} = (\operatorname{grad} \mathbf{v} + (\operatorname{grad} \mathbf{v})^T)/2, \quad (2.3)$$

$$I^2 = \frac{1}{2} \operatorname{tr}(\bar{\mathbf{D}}^2), \quad (2.4)$$

$$p(\rho) = A\left(\frac{\rho}{\rho_0} - 1\right) + B\left(\frac{\rho}{\rho_0} - 1\right)^2. \quad (2.5)$$

In these equations σ_0 is the flow stress of the target material in simple compression, ρ_0 is the mass density of the undeformed target material, A and B are material constants, \mathbf{D} is the strain-rate tensor and $\bar{\mathbf{D}}$ its deviatoric part. Equation (2.5) is obtained from the Tillotson equation by neglecting the parts that apply to hot expanded metal states and the change in temperature of a material point. The constant A is related to the bulk modulus of the material. Equation (2.1) may be regarded as a constitutive relation of a compressible Non-Newtonian fluid with shear viscosity given by $\sigma_0/2\sqrt{3}I$. Equation (2) when substituted into (1.2) gives

$$\begin{aligned} & -\operatorname{grad} p + \frac{\sigma_0}{\sqrt{3}} (\operatorname{div}((\operatorname{grad} \mathbf{v} + (\operatorname{grad} \mathbf{v})^T)/2I) \\ & - \operatorname{grad}((\operatorname{div} \mathbf{v})/3I)) = \rho(\mathbf{v} \cdot \operatorname{grad})\mathbf{v} \end{aligned} \quad (3)$$

which along with (1.1) are the field equations for ρ and \mathbf{v} .

We now non-dimensionalize the variables as follows:

$$\begin{aligned} \bar{r} &= r/r_0, & \bar{z} &= z/r_0, & \bar{\mathbf{v}} &= \mathbf{v}/v_0, & \bar{\boldsymbol{\sigma}} &= \boldsymbol{\sigma}/\sigma_0, & \bar{p} &= p/\sigma_0, & \bar{\rho} &= \rho/\rho_0, \\ \bar{A} &= A/\sigma_0, & \bar{B} &= B/\sigma_0. \end{aligned} \quad (4)$$

Here r_0 is the radius of the cylindrical part of the penetrator, v_0 its speed in the z -direction and the pair (r, z) denotes the cylindrical co-ordinates of a target particle. Hereafter we use only the non-dimensional variables and drop the superimposed bars. Equations (1.1) and (3) in terms of the non-dimensional variables are

$$(\operatorname{grad} \rho) \cdot \mathbf{v} + \rho(\operatorname{div} \mathbf{v}) = 0, \quad (5.1)$$

$$-\operatorname{grad} p + \frac{1}{\sqrt{3}} (\operatorname{div}((\operatorname{grad} \mathbf{v} + (\operatorname{grad} \mathbf{v})^T)/2I) - \operatorname{grad}((\operatorname{div} \mathbf{v})/3I)) = \alpha(\mathbf{v} \cdot \operatorname{grad})\mathbf{v}, \quad (5.2)$$

where

$$\alpha = \rho_0 v_0^2 / \sigma_0 \quad (6)$$

is a non-dimensional number.

† This constitutive relation is discussed briefly in the note at the end of the paper.

For the boundary conditions on the target/penetrator interface we take

$$\mathbf{v} \cdot \mathbf{n} = 0, \quad (7.1)$$

$$\mathbf{t} \cdot (\boldsymbol{\sigma}\mathbf{n}) = 0, \quad (7.2)$$

where \mathbf{n} and \mathbf{t} are, respectively, unit normal and tangent vectors at a point on the interface. The boundary conditions (7) ensure that target particles do not penetrate into the rigid penetrator and the contact surface is frictionless. At points far away from the penetrator nose, we assume that

$$|\mathbf{v} + \mathbf{e}| \rightarrow 0 \quad \text{as} \quad (r^2 + z^2)^{1/2} \rightarrow \infty, \quad z > -\infty, \quad (8.1)$$

$$|\boldsymbol{\sigma}\mathbf{n}| \rightarrow 0 \quad \text{as} \quad z \rightarrow -\infty, \quad r \geq 1. \quad (8.2)$$

In eqn (8.1) \mathbf{e} is a unit vector along the z -axis. This boundary condition states that target particles far from the penetrator but not on the back surface appear to move as a rigid body and those on the back surface are traction free. In order to state the problem precisely one needs to specify the rates at which quantities in eqn (8) decay to zero. We now assume that the nonlinear and coupled equations (5) under the boundary conditions (7) and (8) have a solution and find an approximation to that solution by the finite element method.

FINITE ELEMENT FORMULATION OF THE PROBLEM

For a numerical solution of the problem we first recall that the target deformations are assumed to be axisymmetric and therefore consider the finite region shown in Fig. 1 and

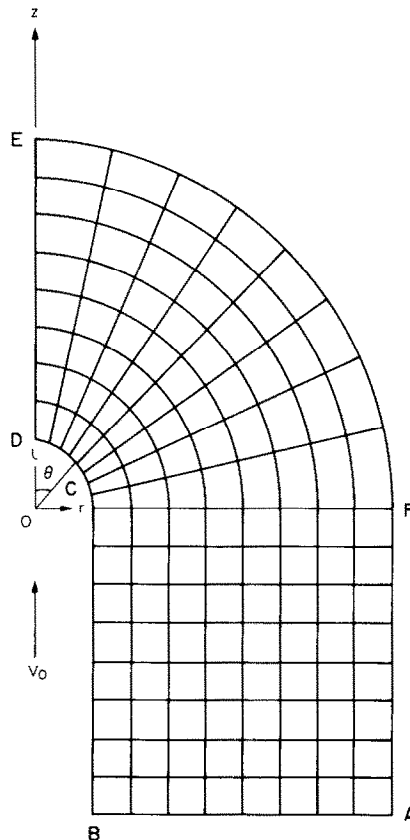


Fig. 1. The finite region studied and its discretization.

impose the following boundary conditions:

$$\sigma_{zz} = 0, \quad v_r = 0 \text{ on the bottom surface AB,} \quad (9.1)$$

$$\mathbf{t} \cdot \mathbf{on} = 0, \quad \mathbf{v} \cdot \mathbf{n} = 0 \text{ on the target/penetrator interface BCD,} \quad (9.2)$$

$$\sigma_{rz} = 0, \quad v_r = 0 \text{ on the axis of symmetry DE,} \quad (9.3)$$

$$v_r = 0, \quad v_z = -1.0 \text{ on the boundary surface EFA.} \quad (9.4)$$

The adequacy of the studied region is verified by ensuring that the computed results especially in the vicinity of the target/penetrator interface are unaffected by the location of the boundary EFA.

Referring the reader to Becker *et al.* [8] for details, we note that a weak formulation of the problem defined on the region R (shown enclosed by ABCDEFA in Fig. 1) by eqns (5) and boundary conditions (9) is that equations

$$\int_R \psi((\text{grad } \rho) \cdot \mathbf{v} + \rho(\text{div } \mathbf{v})) \, dv = 0, \quad (10.1)$$

$$\int_R p(\text{div } \boldsymbol{\phi}) \, dv - \frac{1}{2\sqrt{3}} \int \frac{1}{I} \tilde{\mathbf{D}} : (\text{grad } \boldsymbol{\phi} + (\text{grad } \boldsymbol{\phi})^T) \, dv = \alpha \int_R ((\mathbf{v} \cdot \text{grad})\mathbf{v}) \cdot \boldsymbol{\phi} \, dv, \quad (10.2)$$

hold for arbitrary smooth functions ψ and $\boldsymbol{\phi}$ defined on R such that $\phi_r = 0$ on AB, $\boldsymbol{\phi} = 0$ on EFA and $\boldsymbol{\phi} \cdot \mathbf{n} = 0$ on the target/penetrator interface BCD. In these equations $\mathbf{A} : \mathbf{B} = \text{tr}(\mathbf{A}\mathbf{B}^T)$ for linear transformations \mathbf{A} and \mathbf{B} . Since these equations are nonlinear in \mathbf{v} and ρ , the following iterative technique has been employed. At the i th iteration, equations

$$\int_R \psi((\text{grad } \rho^i) \cdot \mathbf{v}^{i-1} + \rho^{i-1}(\text{div } \mathbf{v}^i)) \, dv = 0, \quad (10.3)$$

$$\begin{aligned} & \frac{1}{2\sqrt{3}} \int_R \frac{1}{I^{i-1}} \mathbf{D}^i : (\text{grad } \boldsymbol{\phi} + (\text{grad } \boldsymbol{\phi})^T) \, dv + \alpha \int_R ((\mathbf{v}^{i-1} \cdot \text{grad})\mathbf{v}^i) \cdot \boldsymbol{\phi} \, dv \\ & = \left[\int p(\rho^{i-1})(\text{div } \boldsymbol{\phi}) \, dv + \frac{1}{3\sqrt{3}} \int_R \frac{1}{I^{i-1}} [(\text{tr } \mathbf{D}^{i-1})\text{div } \boldsymbol{\phi}] \, dv \right] \end{aligned} \quad (10.4)$$

are solved for v^i and ρ^i . The iterative process is stopped when at each nodal point

$$\|v^i - v^{i-1}\| + |\rho^i - \rho^{i-1}| \leq \varepsilon[\|v^{i-1}\| + |\rho^{i-1}|] \quad (10.5)$$

where $\|v\|^2 = v_r^2 + v_z^2$, and ε is a preassigned small number.

The lack of a diffusive term in the balance of mass eqn (5.1) necessitates that the test functions ψ and the trial solutions ρ be chosen from different functional spaces. This is usually referred to as Petrov–Galerkin formulation [9]. We use 9-noded rectangular elements for \mathbf{v} and the four-noded rectangular elements for ρ and employ the basis functions given by Heinrich *et al.* [10] to generate the test functions ψ . These basis functions involve four constants and the rate of convergence of the solution depends rather strongly upon the values of these constants. The test functions $\boldsymbol{\phi}$ and the trial solutions \mathbf{v} are taken from the same space of functions. Thus we have used the Petrov–Galerkin formulation for the continuity equation and the Galerkin formulation for the balance of linear momentum.

COMPUTATION AND DISCUSSION OF RESULTS

A computer code based on eqns (10.3) and (10.4), and employing 9-noded rectangular elements has been developed. The two components of the velocity are taken as unknowns at each node and the mass density is assumed to be unknown only at the four corner nodes. The accuracy of the computer code was established by solving a hypothetical problem involving the flow of a compressible Navier–Stokes fluid in a circular pipe and achieving a favorable comparison between the computed and analytical results. The sample problem studied and the

comparison between the computed and analytical results is given in the Appendix. Even though the formulation of the problem does not require that the mass density be prescribed on any part of the boundary, the numerical solution of the problem necessitated that it be assigned values on a part of the boundary. In the results presented below the non-dimensional mass density was set equal to 1.0 on the part EFA of the boundary. Also the boundary condition $\mathbf{v} \cdot \mathbf{n} = 0$ on the target/penetrator interface BCD was satisfied by using the method of Lagrange multipliers. The finite element discretization of the region studied is depicted in Fig. 1. Note that only one non-dimensional number α governs the deformations of the target material. Thus all of the results below are expressed in terms of α . However the compressibility of the material is governed by the values of A and B in eqn (2.5) which we took as $A = 144.231$, $B = 125.0$. These values, taken from Pidsley's [6] paper, are for aluminum. For a prescribed value of α , the problem was first solved by presuming that the target material is incompressible. This solution for v_r and v_z and $\rho = 1.0$ everywhere was taken as the initial estimate of the solution for the compressible target material. We recall that the basis functions for ψ involve four constants. The number of iterations required to obtain the converged solution depended rather strongly upon the values selected for these constants. In general, however, the number of iterations needed for the solution to converge increased with the increase in the value of α . The parameter ε in the convergence criterion (10.5) was assigned the value 0.04.

In Fig. 2 are plotted the variation of the normal stress, tangential velocity and the second invariant I of the strain-rate tensor on the penetrator nose for $\alpha = 5.36$ and for compressible and incompressible target materials. The compressibility of the target material affects most the values of I near the penetrator nose-tip. Over most of the nose surface the values of I and the normal stress are lower for the compressible target material as compared to that when the

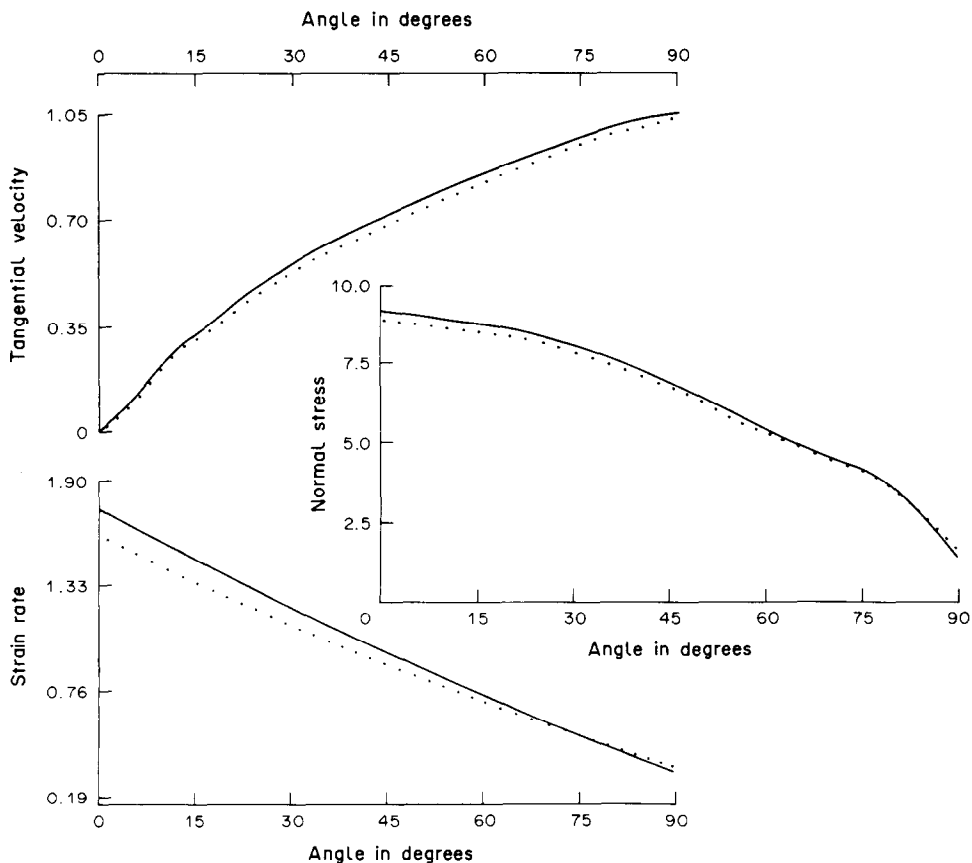


Fig. 2. The variation of the normal stress, tangential velocity and the second strain-rate invariant I on the penetrator nose for $\alpha = 5.36$. — incompressible material, ···· compressible material.

target material is modelled as incompressible. Whereas the peak value of I at the penetrator nose-tip drops by 8.78% when the target material is presumed to be compressible, that of the normal stress decreases by only 3.19%. In the immediate vicinity of the nose tip the tangential velocities for compressible and incompressible targets essentially coincide with each other. However for the angular position θ greater than 12° , the tangential velocity for the compressible target is lower than that for the incompressible target.

Figure 3 depicts the effect of the compressibility of the target material on the variation of the normal stress, strain-rate invariant I and the relative z -velocity along the axial line. As evidenced by the values of I , most of the target deformations occur within a distance of 1.5 times the radius of the penetrator for both compressible and incompressible target materials. In each case the values of I drop off to zero at points on the axial line whose distance from the nose surface is greater than twice the radius of the penetrator. Typically these non-dimensional values of I need to be multiplied by 10^5 to get their dimensional counterparts. Thus peak strain-rates of the order of 10^5 s^{-1} occur for both compressible and incompressible target materials. The values of absolute z -velocity decay to zero a little bit slowly for compressible targets as compared to that for incompressible targets. The rate of decay of the absolute values of σ_{zz} along the axial line in the two cases is nearly the same. The values of $|\sigma_{zz}|$ are less when the target material is modeled as compressible as compared to that when it is taken to be incompressible. The difference between the two values is primarily due to the difference in the values of the hydrostatic pressure in the two cases. For $0 \leq z \leq 2$, this difference in the values of p stayed nearly constant and equalled 0.48.

Figure 4 shows the variation of v_z with r at $z = 0$ and $z = -5.0$ and also the dependence of the axial resisting force F experienced by the penetrator upon α . For both compressible and incompressible target materials the axial resisting force F depends linearly upon α and the two lines are nearly parallel to each other. In each case the dependence of F upon α is rather weak

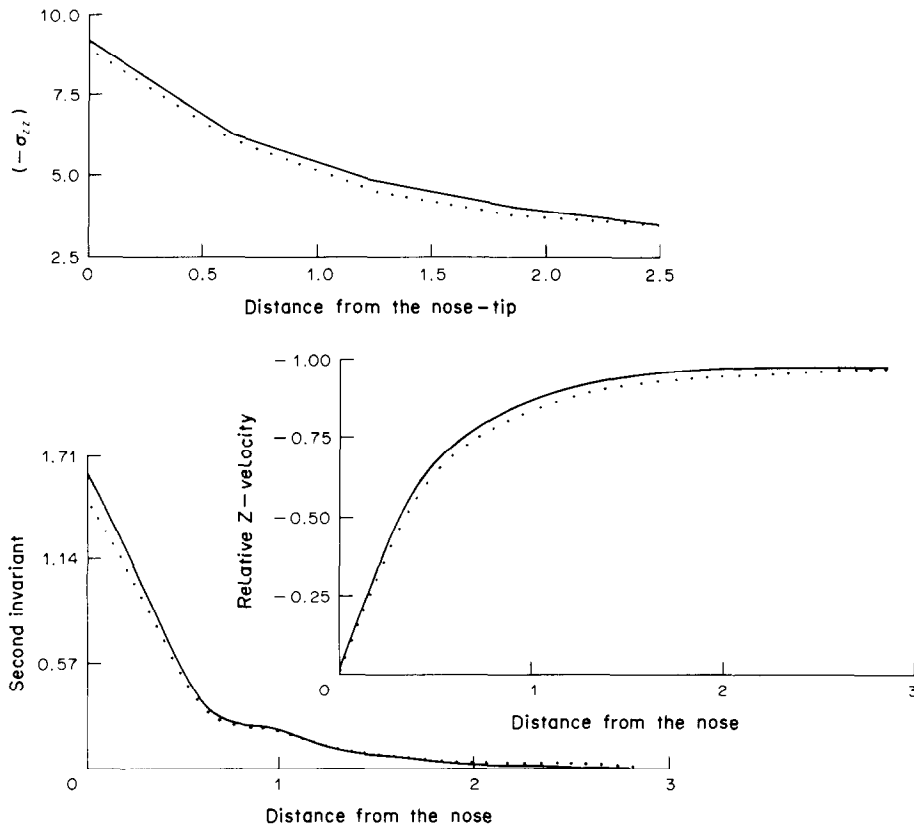


Fig. 3. Variations of $(-\sigma_{zz})$, z -velocity and the second strain-rate invariant I on the axial line for $\alpha = 5.36$. — incompressible material, ···· compressible material.

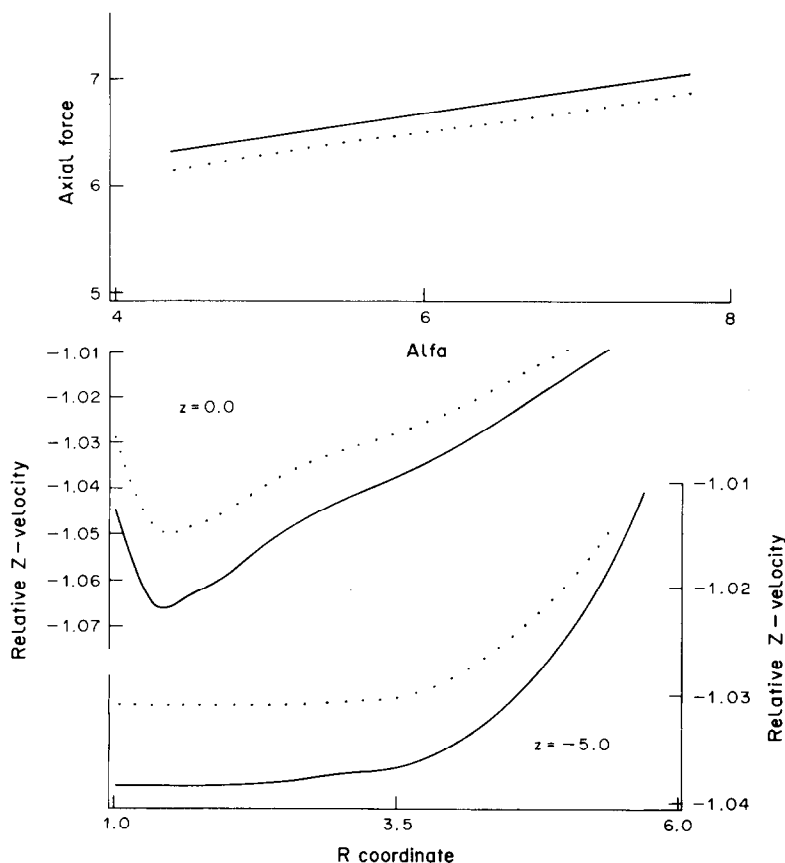


Fig. 4. Dependence of the axial force upon α ; Variations of v_z with r on planes $z=0$ and $z=-5.0$. $\alpha=5.36$. — incompressible material, ···· compressible material.

and explains why the choice of constant target resistance in the simple theory of Tate [2] gives good qualitative results. Note that the dimensional values of F equal $(\pi r_0^2 \sigma_0)$ times its non-dimensional values. The plots of v_z versus r indicate the deformations of the target spread farther to the side of the penetrator than ahead of it. This is true both for compressible and incompressible target materials. Whereas target points on the axial line and ahead of the penetrator situated at a distance of three times the penetrator radius have zero absolute z -velocity, that on the sides of the penetrator and situated at the same distance from the penetrator surface have non-zero z -velocity. The variation of v_z with r on the surface $z=-5.0$ indicates that the material in the region $1 \leq r \leq 3.5$ extrudes as a rigid block.

The value of the compression c , defined as $(1 - \rho^{-1})$, at the nose tip was found to depend linearly upon α , and for $4 \leq \alpha \leq 8$ the two are related by

$$c = (4.75 + 0.575\alpha)/100.$$

After having delineated the difference in the solutions for compressible and incompressible target materials we next studied the effect of the penetrator speed upon the deformations of the compressible target. We recall that the corresponding results for the incompressible target material have been given by Batra and Wright [3]. Results presented in Fig. 5 indicate that the speed of the penetrator has virtually no effect on the tangential velocity of the target particles abutting the penetrator hemispherical nose. However, the normal stress does increase with α on most of the nose surface except near its periphery where the normal stress decreases with α . The normal stress at $\theta = 65^\circ$ seems to be affected little by the values of α . Such a behavior was also observed at $\theta = 45^\circ$ for incompressible target materials [3]. The peak value of the normal stress, which occurs at the penetrator nose tip, increases from 7.25 to 9.5 when α is increased from 2.35 to 6.12. Whereas in the previous work [3], for $\alpha = 6.13$ the target particles seemed to

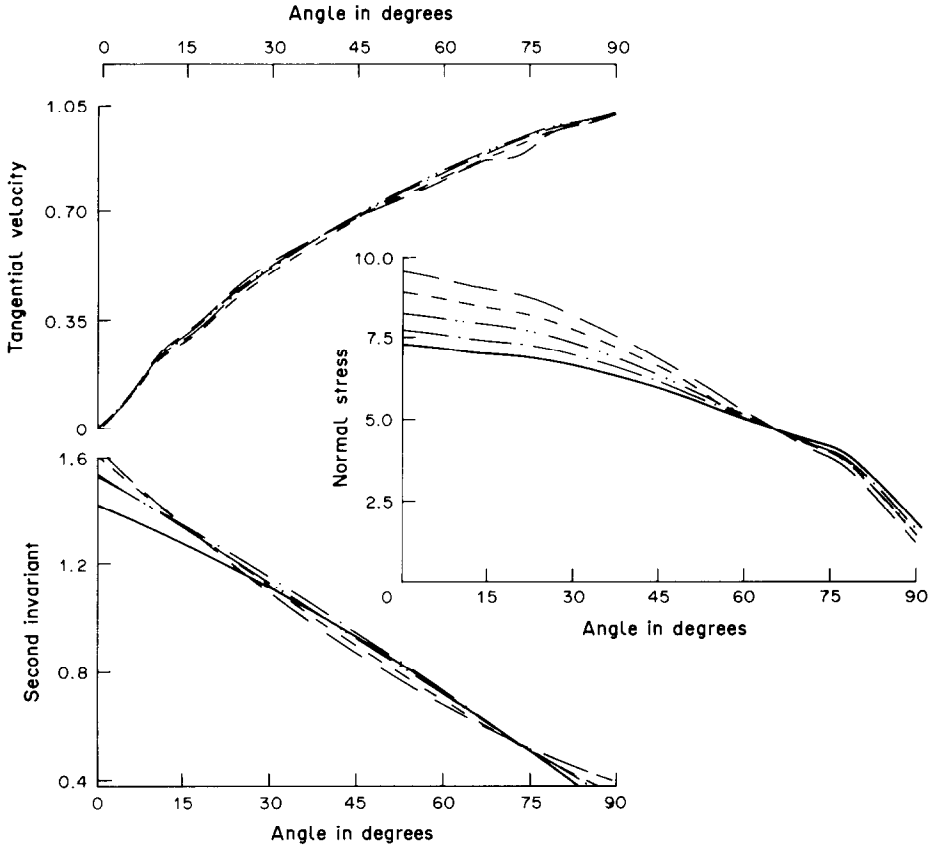


Fig. 5. Distribution of the tangential velocity, normal stress and the second strain-rate invariant on the hemispherical nose of the penetrator for different values of α and compressible target material. — $\alpha = 2.63$; - - - $\alpha = 3.44$; - - - - $\alpha = 4.35$; - - - - - $\alpha = 5.36$; - - - - - $\alpha = 6.49$.

separate away from the penetrator nose surface near its periphery, no such behavior was observed in the present case. The finite element mesh used herein is finer than the one employed earlier. Also the mass density is taken as the independent variable here whereas in [3] the hydrostatic pressure p was taken as an independent variable because of the assumption of incompressibility. The values of the second strain-rate invariant in the vicinity of the penetrator nose tip are affected most by α but those at points for which $20^\circ \leq \theta \leq 70^\circ$ seem to be affected less. The increase in the value of the normal stress on the penetrator nose with α occurs primarily because the hydrostatic pressure p increases with α .

In Fig. 6 is plotted the effect of α upon the variation of v_z , $(-\sigma_{zz})$ and I at target particles on the axial line ahead of the penetrator. The penetrator speed does not affect to any noticeable degree the values of I and v_z . However, the values of $(-\sigma_{zz})$ at points on the axial line increase with α ; this increase is mainly due to the higher values of p . For all values of α considered here the target particles within a distance of almost three times the penetrator radius undergo deformations; those outside this region hardly deform.

On the axial line nearly uniaxial strain conditions prevail. Thus the magnitude of the deviatoric stress s_{zz} , defined as $p + \sigma_{zz}$, should equal $2/3$ the flow stress. For points on the axial line for which $0.0 \leq z \leq 1.5$, and for $\alpha = 5.36$, s_{zz} was computed to be 0.771 and 0.741 for compressible and incompressible materials, respectively.

We note that the region studied is adequate since the target particles within a distance of one penetrator radius of the boundary EFA hardly deform and the deformation of particles situated within one penetrator radius of the boundary surface AB are independent of z .

We are not aware of any experimental work available in the open literature with which we could compare our computations. Nevertheless, the kinematic and stress fields found in this

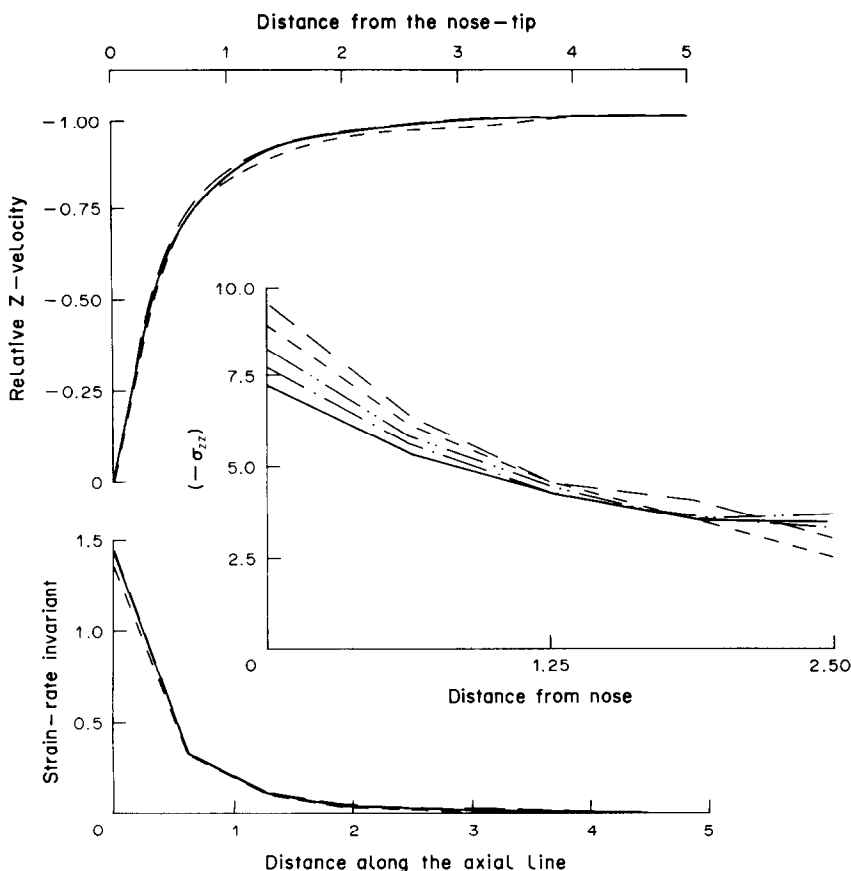


Fig. 6. Variation of the z -velocity, $(-\sigma_{zz})$ and the second strain-rate invariant I along the axis ahead of the penetrator for different values of α and compressible target material. See Fig. 5 for explanation.

study should help in devising or checking the results from simpler theories of target deformations.

CONCLUSIONS

For the same speed of the rigid cylindrical penetrator with a hemispherical nose, the peak values of the strain-rate invariant and the normal stress, both of which occur at the target particle situated at the penetrator nose-tip, are lowered by 8.78 and 3.19%, respectively, for compressible target materials as compared to that for incompressible materials. The axial resisting force experienced by the penetrator is nearly 10% less when the target material is compressible as compared to that when it is incompressible.

Both for compressible and incompressible target materials, significant deformations occur only at points that are less than three penetrator radii from the penetrator, and the target seems to deform farther to the side than ahead of the penetrator. In each case the target material adjacent to the sides of the penetrator appears to extrude rearwards as a uniform block that is separated from the stationary target by a deforming region.

Note added in proof

Recent unpublished work by Batra and Liu involving dynamic plane strain simple compression of viscoplastic solids defined by the constitutive relation (2.1) has shown that, for short times after the application of the load, material lines in a direction perpendicular to the axis of the compressive load are also shortened. The constitutive relation

$$\boldsymbol{\sigma} = -p(\rho)\mathbf{1} + \frac{\sigma_0}{\sqrt{3}I} \mathbf{D} \quad (\text{N1})$$

with I defined by eqn (2.4) rules out this anomalous behavior. The constitutive relation (N1) can be rewritten as

$$\boldsymbol{\sigma} = -\left(p(\rho) - \frac{\sigma_0}{\sqrt{3}I} \text{tr } \mathbf{D}\right)\mathbf{1} + \frac{\sigma_0}{\sqrt{3}I} \bar{\mathbf{D}}. \tag{N2}$$

Thus, for a given \mathbf{D} , eqns (2.1) and (N1) give identical values of the deviatoric stress.

For the steady state problem studied herein, constitutive relations (2.1) and (N1) give essentially the same results.

Acknowledgement—This work was supported by the U.S. Army Research Office contract DAAG29-85-K-0238 to the University of Missouri-Rolla.

REFERENCES

[1] V. P. ALEKSEEVSKII, *Combust. Expls Shock Waves* **2**, 63 (1966).
 [2] A. TATE, *J. Mech. Phys. Solids* **15**, 387 (1967).
 [3] R. C. BATRA and T. W. WRIGHT, *Int. J. Engng Sci.* **24**, 41 (1986).
 [4] R. C. BATRA, *Int. J. Engng Sci.* **25**, 1131 (1987).
 [5] R. C. BATRA, *Comput. Mech.* **3**, 1 (1988).
 [6] P. H. PIDSLEY, *J. Mech. Phys. Solids* **32**, 315 (1984).
 [7] L. J. HAGEMAN and J. M. WALSH, *HELP, A Multi-Material Eulerian Program for Compressible Fluid and Elastic-Plastic Flows in Two Space Dimensions and Time*. Systems Science and Software Report 3SR-350 (1971).
 [8] E. BECKER, G. CAREY and J. T. ODEN, *Finite Elements—An Introduction*, Vol. 1. Prentice-Hall, Englewood Cliffs, N.J. (1981).
 [9] T. J. R. HUGHES, *The Finite Element Method. Linear Static and Dynamic Finite Element Analysis*. Prentice-Hall, Englewood Cliffs, N.J. (1987).
 [10] J. C. HEINRICH, P. S. HUYAKORN and O. C. ZIENKIEWICZ, *Int. J. Num. Meth. Engng* **11**, 131 (1977).

(Received 29 October 1987)

APPENDIX

In order to assess the validity of the developed finite element code and establish the reliability of the computed results we solved the following problem for compressible Navier–Stokes fluids. We replaced eqn (2.1) by

$$\boldsymbol{\sigma} = -p(\rho)\mathbf{1} + \bar{\mathbf{D}}, \quad p(\rho) = \rho/100 \tag{A1}$$

and the balance of linear momentum (1.2) by

$$\text{div } \boldsymbol{\sigma} = \boldsymbol{\rho}(\mathbf{v} \cdot \text{grad } \mathbf{v}) + \mathbf{b} \tag{A2}$$

where \mathbf{b} is the body force per unit mass. The fields

$$v_r = r^2/2, \quad v_z = -rz/2, \quad \rho = (z^2 - 1/r^2)/4, \tag{A3}$$

with

$$b_r = \frac{r^{-3}}{200} + \frac{r^3 z^2}{8} - \frac{r}{8} - \frac{11}{12}, \quad b_z = \frac{z}{200} + z/4r \tag{A4}$$

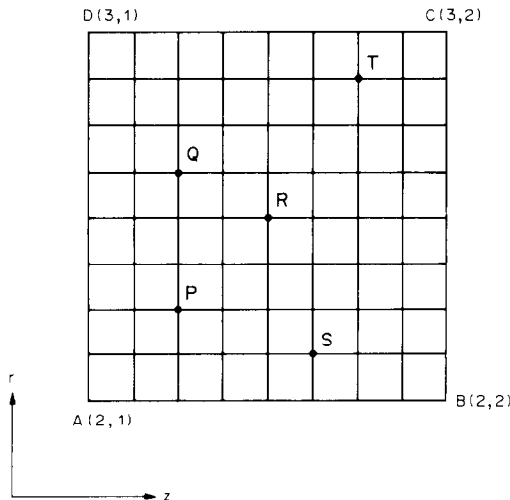


Fig. A1. The finite element grid for the sample problem.

Table A1. Comparison of analytical and numerical solution

Point	Analytical values			Computed values			% Difference		
	v_r	$-v_z$	ρ	v_r	$-v_z$	ρ	v_r	v_z	ρ
P	2.53125	1.40625	0.34124	2.53077	1.43358	0.342852	0.019	1.944	0.472
Q	3.44531	1.64063	0.35435	3.4588	1.68613	0.359417	0.391	2.774	1.432
R	3.125	1.8750	0.52250	3.11498	1.91764	0.52810	0.321	2.274	1.072
S	2.53125	1.82813	0.61077	2.50815	1.85314	0.618034	0.913	1.368	1.189
T	3.78125	2.57813	0.84585	3.76938	2.59881	0.838507	0.314	0.803	0.868

satisfy the balance of mass and the balance of linear momentum. Values of v_r and v_z as given by the presumed fields were assigned on the boundary faces BC, CD and DA of the domain shown in Fig. A1; those of v_r and σ_{zz} were prescribed on AB and values of ρ were prescribed on AD and DC. Note that b_r and b_z would appear on the right-hand side of eqn (10.4) and their values, as given by eqn (A4), were input into the computer code. In Table A1 are compared the values of v_r , v_z and ρ as computed from expressions (A3) and the computer code with ϵ in eqn (10.5) set equal to 0.005. It took 10 iterations for the solution to converge. The maximum error in v_r , v_z or ρ at any of the node points was found to be less than 3.25%.